Experimental Investigation of Spray Combustion Regimes in Aero-Engine Combustors

M. Vicentini[⋆,†], R. Lecourt[⋆], O. Rouzaud[⋆], V. Bodoc[⋆], O. Simonin[⋆⋆]

[⋆]*ONERA*
2 Avenue Edouard Belin, Toulouse cedex 31000, France
[⋆⋆]*IMFT*
Allée du Professeur Camille Soula, Toulouse cedex 31400, France
· · ·
[†] maxime.vicentini@onera.fr

Abstract

At ONERA Fauga-Mauzac center, a new air-breathing propulsion test setup, Prométhée-LACOM, has been recently developed. In this paper, both non-reacting and reacting two-phase flows were investigated. In reacting two-phase flow, simultaneous OH-PLIF and Mie scattering imaging were implemented in order to characterize the flame structure. The different behaviours observed in this study seem to support the existence of spray combustion regimes. Moreover, statistical analysis were performed on the spatial distribution of droplets and indicated that the centre-to-centre inter-droplet distance (nearest neighbour) could be described by means of a Log-Normal distribution.

1. Introduction

Turbulent combustion is widespread in engineering applications such as gas turbines, internal combustion engines, rocket motors and still contributes significantly to our energy supply. Typically in aeronautical propulsion devices, liquid fuels - with high energy density - are used in order to optimize storage volumes and then increase ranges of aircraft. At the inlet of the combustion chamber, the liquid fuel must be atomized into a spray of small droplets to increase the exchange surface area between fuel and hot gases. Actually, the combustion efficiency depends strongly on the quality of fuel pulverization, fuel-oxidant mixing and chemical kinetics processes. Even though the specific fuel consumption of recent turbofan engines has decreased, pollutant emissions levels remain high and are increasingly subject to environmental taxes in the transport sector (NO_x, CO, UHC). Because of this major issue, investigations of spray combustion are quite numerous.

Chiu [1] and Chigier [2] developed the pioneer concept of "spray combustion regimes". According to their theory, within dense zones of a cloud, the droplets vaporize collectively and the front flame stands beyond the outer boundary of the spray. Indeed, the core of those zones is non-flammable because of a too-rich-fuel mixture. In contrast, when the droplet spacing is sufficiently great, then hot gases and oxidant can penetrate into the cloud and potentially ignite single droplets. Thus, in an intermediate number density of droplets a "Group Combustion" regime is likely - diffusion flame enclosing cluster of droplets. Most of available works are aimed at theoretical and numerical analysis - see for example Correa [3], Annamalai [4], Candel [5], Reveillon [6]. Unfortunately, experimental investigations on this topic are less common. Akamatsu and coworkers [7-8] studied a premixed spray flame stabilized by an annular hydrogen flame pilot. They implemented simultaneous local measurements such as Phase Doppler Anemometer (PDA) and photomultipliers (Mie scattering, and light emission of OH- and CH-radicals). The authors found that the uniformly premixed spray stream was fragmented into droplet clusters due to preferential through easy-to-burn routes in the reacting flow. More recently, Beck and Koch [9-10] studied a partially prevaporized swirl-stabilized spray flame. They used CH-PLIF and Mie scattering visualizations in order to capture single droplet burning modes. Besides, 3D-Phase Doppler Anemometer permitted measuring the slip velocities of droplets. Two modes were identified: envelope flame and wake flame, depending on the slip velocity. Finally, the authors suggested that wake flames produce less NOx emissions than envelope flames due to an increase of the mixing length between the surface of the droplet and its flame.

In this article, we focus on the experimental study of those spray combustion regimes. In this purpose, a new air breathing propulsion test setup has been developed. In the first part (section II), we present the test setup design

which is particularly suitable for optical measurements in order to characterize spray combustion. The configuration is rather academic but has representative features of the flow in an actual aero-engine combustor. Subsequently, the implementation of measurements is described. An important point concerns the setting of simultaneous optical techniques to obtain superimposed visualizations of both droplets and reacting zones. Section III presents the results of both non-reacting and reacting flow. The aim is to build an experimental database to improve combustion models by using numerical simulations. Moreover we underline combustion effects on the flow behaviour - gaseous phase instabilities, droplet sizes and velocities - compared to the non-reacting flow. A specific analysis on the spatial distribution of droplets under reactive conditions is also carried out. By doing so, spray heterogeneities are highlighted and droplet spacing distributions are described by means of a probability density function. Furthermore, experimental evidences supporting the existence of spray combustion regimes are provided. It seems that the inter-droplet distances play a major role in the appearance of those behaviours.

2. Materials and Methods

2.1 Test Setup

An Overview

At ONERA Fauga-Mauzac center, a new air-breathing propulsion test setup, Prométhée-LACOM, has been recently developed (see Fig. 1(l.)). The air feeding system is made up of a spherical pressure vessel (25 bar), gas pressure regulators and an electric heater (1 MW). The air mass flow rate is measured with a sonic nozzle located downstream of the electric heater (± 3.3 % accuracy). Subsequently, the preheated air stream passes through a succession of flow conditioners and grids for generating turbulence. The test chamber consists of a square internal section (120 x 120 mm^2). As it can be seen from Fig. 1(r.), the confined turbulent air stream flows around a fuel injection system prior to the combustion chamber. The injection system consists in a bluff-body in which a liquid fuel nozzle is mounted. It should be noted that the bluff-body crosses the test section over the entire width. The fuel feeding line (1.5 MPa) is equipped with a Coriolis flowmeter (± 0.2 % accuracy). The spray nozzle is centered and screwed into the rear face of the bluff-body. As illustrated in Fig. 1(r.), a spray of droplets is generated downstream directly into the combustor. The fuel injector consists in a flat fan nozzle which produces an elliptical-shaped spray. In addition, the opening angles of the major and minor axis are respectively 150° and 25°. The wide angle is set up so as to spray towards the upper and lower walls of the combustor. The water-cooled combustor is equipped with 3 interchangeable UV-transparent windows allowing to perform optical measurements downstream of the injection system. Ignition of the air-fuel mixture is triggered by a hydrogen-oxygen torch. Finally, the burnt gases are ejected in the exhaust pipe.
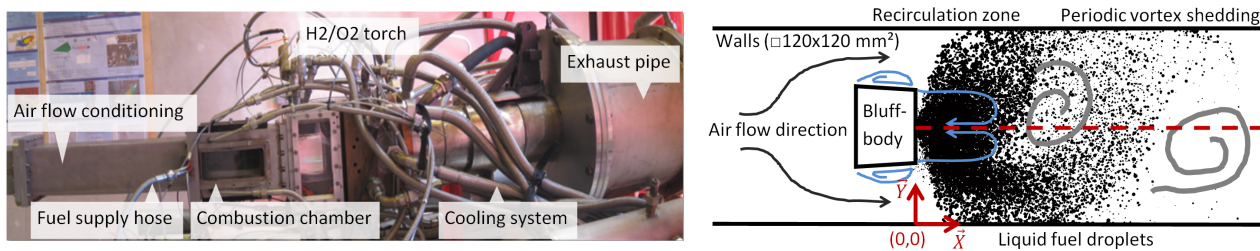

Figure 1 – The test setup - Picture of the facility **(left)** - Illustration of the non-reacting two-phase flow **(right)**

Specific Features

A previous sizing study has been carried out on a prototype in 1:1 scale to choose the bluff-body geometry [15]. For a 6 m/s inert mean airflow velocity at 298 K, a vortex-shedding phenomenon is observed downstream of the bluff-bodies. The study highlights establishment of a periodic generation of eddies with opposite sense of rotation, so called a von Kármán vortex sheet. As a result, a trapezoidal bluff-body with 42 % ratio blockage is chosen as optimal geometry in terms of constancy of Strouhal number and signal intensity. At such conditions, the Particle Image Velocimetry measurements (PIV) reveals a main recirculation zone in the bluff-body's wake, as illustrated in Fig. 1(r.). The average recirculation length is approximately equal to the bluff-body's height (50 mm).

Because of its bi-dimensional design, the experimental setup generates a turbulent flow with two-dimensional

mean properties. Moreover, the flat spray of droplets is mainly located around the vertical mid-plane of the combustor. So, as the experimental diagnostics are either punctual or planar (imaging devices), the configuration ensures the measurement of spatially correlated flow data (droplet positions, sizes, velocities and flame position, intensity). Furthermore, in the Prométhée-LACOM test setup, the main features of a flow in an actual aero-engine combustor are preserved. Indeed, the air flow is confined, turbulent and exhibits instabilities and large-scale structures. Besides, the flame is anchored aerodynamically by creating a main recirculation zone.

The *n*-decane is selected as surrogate fuel because it has chemical properties close to kerosene ones (density, surface tension, auto-ignition temperature). The droplet spray generated is polydisperse (droplets from 5 to 150 μm). Finally, the experiments replicate the operating lean-burn conditions of a turbofan engine, during a flight phase at cruising speed, in terms of fuel-air equivalence ratio.

2.2 Operating conditions

In this paper, both non-reacting and reacting two-phase flows are investigated. The nominal operating point is set at an air mass flow rate equal to 64 g/s. At the combustor inlet, the air flow is at standard atmospheric pressure and 450 K. The corrected mass flow rate corresponds to 1.36 kg.s^{-1}. $\sqrt{K}$.bar^{-1}. Since the combustion section is 120 x 120 mm^2, the mean airflow velocity is about 6 m/s. Consequently, the Reynolds number based on the hydraulic diameter is about 22 000. The liquid fuel temperature is measured just upstream from the nozzle and is equal to 330 K. Then the fuel ($C_{10}H_{22}$, 95 % purity) is injected at 1 g/s to provide a 44 kW thermal power. Therefore, the fuel-air equivalence ratio is around 0.24. The water cooling of the combustion chamber protects the inner walls (< 650 K) to perform long series of tests (several tens of minutes).

2.3 Implementation of measurements

Main measurements

The challenge of this experimental programme is to build a new database in two-phase flow combustion with the purpose to validate physical models and numerical simulations. To do so, the gaseous phase and the liquid phase are studied in non-reacting and reacting flow. Table 1 summarizes the main measurements implemented for the test setup. The Particle Image Velocimetry measurements (PIV) which allow to assess the velocity fields of the seeded gaseous phase, are the subject of a previous measurement campaign [15]. The pressure measurements are used to characterize the instabilities of the gaseous phase in the combustor. The chemiluminescence and Planar Laser-Induced Fluorescence (PLIF) imaging are employed to study the flame fronts in the reacting flow. The first technique uses spontaneous chemical excitation of a flame marker unlike the second technique which produces excitation of the marker by means of a laser. Droplets illuminated by a laser sheet generate light Mie scattering. This signal can be captured by a camera in order to evaluate the positions of droplets from images. Finally, application of a two-components Phase Doppler Interferometry technique (PDI) allows to measure simultaneously the instantaneous droplet velocities (longitudinal, transverse) and their sizes. For more details on spray diagnostics, we recommend the lecture of Bachalo's paper [16].

Table 1 – Sequence of experiments

Conditions	Gaseous phase	Liquid phase
Non-reactive	PIV Pressure tap	PDI Mie scattering
Reactive	Pressure tap Chemiluminescence OH* OH-PLIF	PDI Mie scattering

Synchronized measurements using a reference signal - Non-reactive conditions

In order to characterize the non-reacting flow, simultaneous measurements on the gaseous phase and the liquid phase are carried out. Indeed, the pressure fluctuations signal at the level of bluff-body, is used as reference signal

(timebase). Actually, the bluff-body is drilled on its upper and lower faces of static pressure holes (1.7 mm diameter). Fluctuations of differential pressure between the upper and lower faces are measured by a diaphragm pressure transducer (± 0.86 kPa sensitivity). Moreover, this signal is sampled at 40 kHz on the data acquisition system of the test bench. In parallel, the liquid phase is characterised with either Phase Doppler Interferometry (PDI) or light Mie scattering by droplets. Thus, a post-processing program links the data with the timebase - a posteriori agreement for clock synchronization. Lastly, a phase-averaging is applied on the measurements to relate the unsteadiness of droplets dispersion with regards to the dynamic behaviour of the gaseous phase.

Simultaneous visualizations of OH-PLIF and Mie scattering - Reactive conditions

The aim is to describe the flame structure and to highlight the existence of spray combustion regimes in the reacting two-phase flow. For this purpose, simultaneous tomographic visualizations on the reactive continuous phase and the dispersed phase are conducted with a high spatial resolution. The synchronization system of Planar Laser-Induced Fluorescence from hydroxyl radicals (OH-PLIF) and Mie scattering measurements is shown Fig. 2. Firstly, to excite OH radicals, a millimetric thin UV laser sheet (λ = 282.69 nm) is generated at the outlet of a tunable dye laser Quantel TDL+, pumped by a Nd:YAG laser Quantel YG 980. Secondly, to illuminate droplets, a millimetric thin visible laser sheet is produced from the outlet of a high-frequency Nd:YLF laser Quantronix Darwin (λ = 527 nm). The UV light sheet crosses the combustion chamber from the top window whilst the visible laser sheet crosses from the bottom window. The two light sheets are superimposed along the droplet spray axis over a 100 mm distance. To acquire the OH fluorescence images, an intensified CCD camera PI-MAX 2 is focused perpendicularly on the face of the laser sheets through the combustor's lateral window. The camera is equipped with a band-pass filter centred at 311 nm ± 5 nm. Likewise, a high-speed camera Phantom V341 is positioned aside to capture the Mie scattering of droplets. The angular separation between both video cameras is 11°. A dewarping procedure enables superimposition of the stack of OH-PLIF and Mie scattering visualizations. A maximal spatial deviation of 57 μm is measured between the two series of images. The useful overlapping area of both video cameras is equal to 51.2 x 45.6 mm^2 corresponding to a 1804 x 1606 px^2 corrected resolution (35.2 px/mm).

A computer is used for triggering the temporal synchronization of both optical techniques. Signal conditioning is applied to electronic camera signals before to be digitized on the data acquisition system (40 kHz). The digital timing diagram is illustrated Fig. 2. The falling edge of the "Ready" signal corresponds with the beginning of the data recording. From this instant each falling edge of the "TTL Mie" is associated with a visible laser flash and consequently a Mie scattering image (every 1 ms). Similarly, each rising edge of the "TTL LIF" signal is associated with an UV flash laser and thus with an OH-PLIF image (every 250 ms). The synchronization system is set to provide a cyclic matching of a falling edge "TTL Mie" with a rising edge "TTL LIF". As a result, a new couple of visualizations is obtained. On the overall network, a maximal 2 μs jitter can exist on the image matching time.
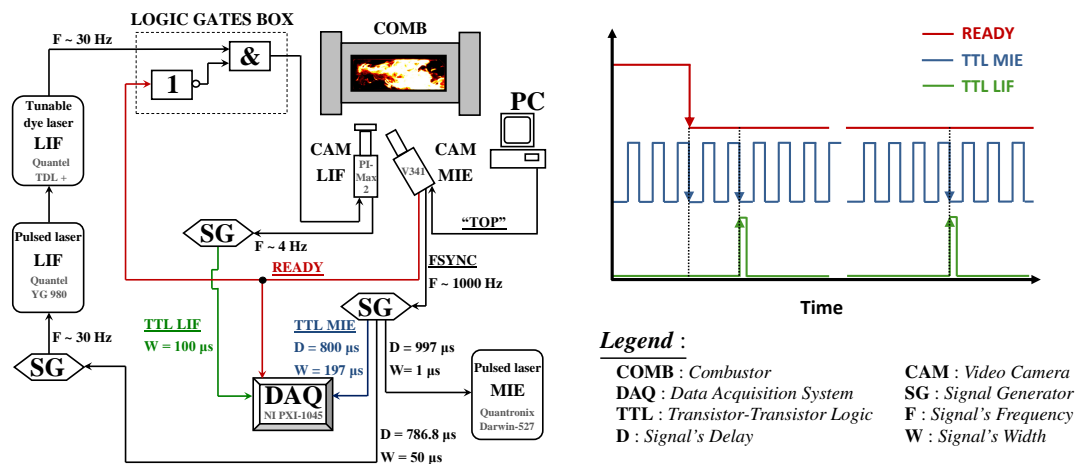

Figure 2 – Setting and digital timing diagram for the synchronization of OH-PLIF and Mie scattering imaging

3. Results

3.1 Spectral Analysis

A spectral analysis of the reference signal - fluctuations of pressure at the level of the bluff-body - is conducted under the operating conditions. Fig. 3(l.) depicts the normalized power spectral densities for the one-phase non-reacting flow, the two-phase non-reacting flow and the two-phase reacting flow. For the non-reacting case, both spectrums (black and blue) are practically superimposed. Moreover, the same narrowband peak frequency at 38 Hz is highlighted. Thus, the Strouhal number based on the height of the bluff-body and the mean velocity is equal to 0.32. Likewise, by applying a fast Fourier transform (FFT) algorithm on the instantaneous transverse droplet velocities (V_y) from PDI measurements, an identical Strouhal number is obtained.

The droplet segregation can be characterized from the Stokes number :

$$\text{St} = \frac{\rho_l . d_{10}^2}{18\mu_{air}} f_g \tag{1}$$

where ρ_l is the density of the liquid fuel, μ_{air} the air dynamic viscosity, d_{10} the arithmetic mean diameter of droplets and f_g the global frequency mode. Under those conditions, the Stokes number is less than 1 for droplets smaller than 130 μm. Actually, the arithmetic mean diameter is about 30 μm and hence the Stokes number is approximatively equal to 6.10^{-2}. So, most of the droplets are supposed to follow the gas closely. Therefore, the peak frequency corresponds with the von Kármán hydrodynamic instabilities which generate periodic fluctuations of pressure on the bluff-body's faces and scatters the droplets downstream. The vortex shedding phenomenon is not much perturbed by the liquid droplet loading. Fig. 3(r.) shows the phase-averaging of the Mie scattering visualizations. It should be noted that the phase-averaging is made upon 160 images per phase with an accuracy ± 4°. Despite a spray asymmetry, the global periodic dispersion of droplets by large-scale structures is also revealed by doing so. Actually, the droplet spray asymmetry is due to a manufacturing defect of the nozzle which sprays a greater quantity of fuel to the bottom of the combustor.

In the reacting flow, nevertheless, the global frequency mode is suppressed - the peak frequency is no longer observable. This effect has been already disclosed in bluff-body premixed flames [12-13]. Furthermore, the power spectral density is greater in non-reacting cases because of the heat released by combustion in the flow. One can see on PDI velocity profiles (longitudinal and transverse), Fig. 5, that the droplets are accelerated in the reacting flow compared to the non-reacting flow. Actually, at 53 mm from the nozzle on the central axis, the average longitudinal velocity of droplets is approximatively equal to the mean airflow velocity under non-reactive conditions (6 m/s). In the reacting flow, the average longitudinal velocity of droplets is multiplied by a factor 3. This can be explained by the expansion of the gaseous phase due to combustion (ratio of densities between inert and reacting flow). To conclude, under those operating conditions, the heat released by combustion is sufficiently high to cause an increase in temperature, a gas expansion and an acceleration of the flow field up to the complete vanishing of vortex shedding.
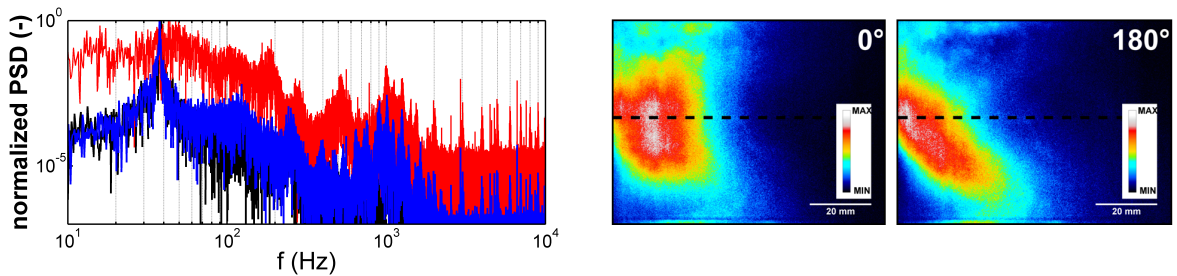

Figure 3 – Normalized power spectral densities [**black** and **blue** : respectively non-reacting one- and two-phase flow, **red** : reacting two-phase flow] **(left)** - Phase-averaging of Mie scattering images in non-reacting two-phase flow **(right)**

3.2 Global flame structure

To determine the global flame structure, the release of OH* radicals is captured by chemiluminescence. A band-pass filter centred at 311 nm ± 5 nm is used. This filter has a maximal transmission of 50 %. In order to offset the light intensity, a Lamber HiCATT image intensifier is mounted between the high-speed camera Phantom V341 (1 kHz) and the system lens plus filter. Averaging the instantaneous OH* chemiluminescence visualizations, as shown Fig. 4(r.),

over 4 seconds (4 000 images), provides a global view of the flame structure presented in Fig. 4(l.). The anchored flame is heart-shaped, or M-shaped, due the recirculation zone of the bluff-body's wake. One can see that chemiluminescence intensity is not symmetric with respect to the central axis of the combustion chamber (Y = 60 mm). Indeed, the heat released in the reacting zone is higher at the bottom of the combustor. Besides, on the average droplet velocity and size profiles, at 9 mm downstream of the nozzle, this asymmetry can also be observed. Those effects support the assumption of a manufacturing defect of the nozzle as discussed previously.
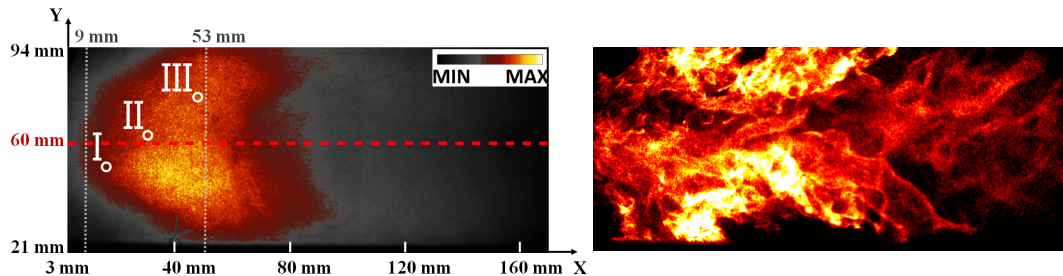

Figure 4 – Time average of OH* chemiluminescence images **(left)** - Typical instantaneous of OH* chemiluminescence visualization **(right)**

3.3 Droplet size distributions and velocities

Two PDI measurements sections, in the mid-axis of the combustion chamber, are investigated. As a result, the average longitudinal and transverse velocities of droplets and their arithmetic mean diameters are plotted in Fig. 5. Because of the height of the combustor's windows, the sections are limited between Y = [32 ; 82] mm. The spatial measurement discretization is equal to 2 mm for the non-reactive case and 4 mm for the reactive case. The first section is located at 9 mm downstream from the fuel nozzle. Under reactive conditions, this section is just upstream the average position of the flame, as seen Fig. 4(l.). The second section is located at 53 mm downstream the injector and inside the flame region.

It should be noted that for all measuring points of the PDI database, the droplet size distributions can be described by means of Log-Normal distributions. On the central axis, at 9 mm downstream from the injection face, the arithmetic mean diameter (d_{10}) and the Sauter mean diameter (d_{32}) are respectively 31 μm and 48 μm for the non-reacting flow as opposed to 38 μm and 51 μm for the reacting flow. Firstly, the minimum and maximum sizes of droplets increase with the temperature. Besides, the increase of the minimum size is more important than the increase of the maximum size. Secondly, the coefficient of variation - defined as the ratio of the standard deviation to the mean - is lower for reacting case than non-reacting case, which means that the dispersion on droplet size is less significant. Thirdly, the moment coefficient of skewness - or the third standardized statistical moment - is smaller in the reacting flow, so the size droplet distribution is straightened towards the biggest droplet sizes and becomes more symmetric around the arithmetic mean diameter. Lastly, the sample excess kurtosis - defined as the fourth standardized statistical moment - is also reduced under reacting conditions, which suggests that the droplet size distribution has a more rounded peak around the arithmetic mean diameter. Moreover, it implies thinner tails, thus the distribution becomes narrower as surrounding gas temperature increases. Those tendencies can be explained by the fact that in the reacting flow the smallest droplets are vanishing more rapidly than the increase of the evaporation of the biggest ones.

One observes from the arithmetic mean diameter profiles that the droplets which cross the flame (at 53 mm) are smaller compared to the droplets located just upstream the flame (at 9 mm). Moreover, the 53 mm section corresponds with the intersection of the d_{10} profiles under the non-reactive and reactive conditions. So, in the reacting flow the droplets evaporate more rapidly due to their crossing in the flame. Further away in the flame, we expect to achieve even more small droplets.

At 53 mm from the nozzle, the average longitudinal velocity is flatter than at 9 mm (for the two conditions). Indeed the flow is more uniform because it is less influenced by the bluff-body's wake. Moreover the droplets are likely in equilibrium with the gaseous phase.

3.4 Spatial distribution of droplets

The droplet distribution is of fundamental importance in understanding of physical mechanisms taking place in combustor sprays. The aim of this section is to characterize the statistical spatial distribution of fuel droplets in the
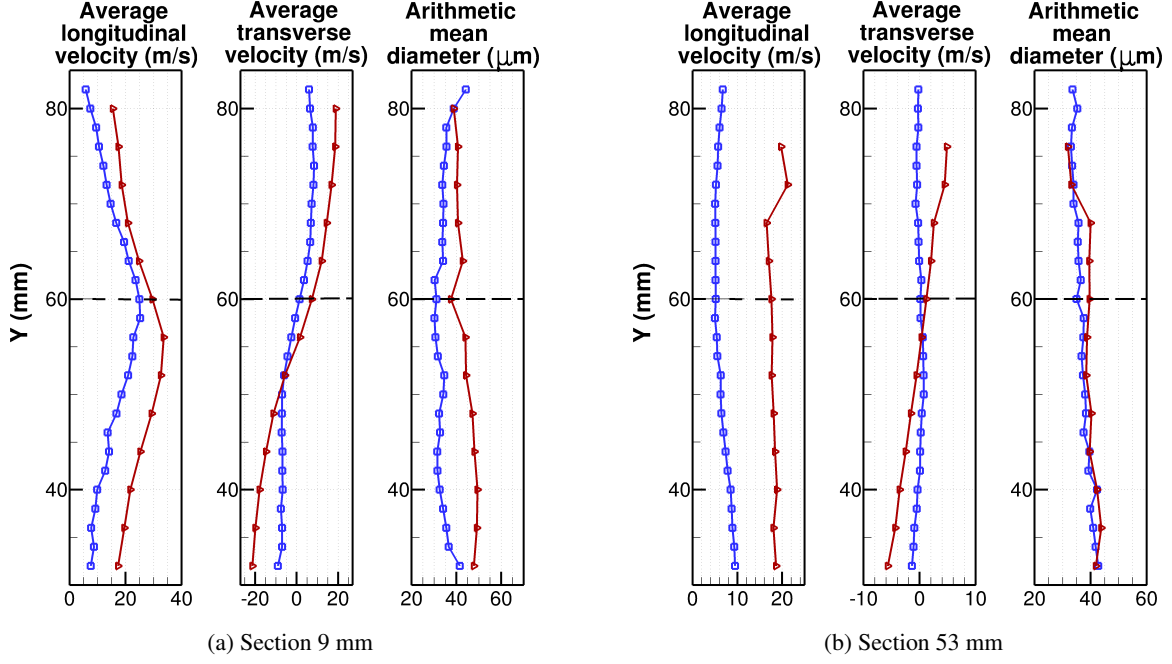
(a) Section 9 mm   (b) Section 53 mm

Figure 5 – PDI measurements sections - □ : non-reacting two-phase flow, ▷ : reacting two-phase flow

reacting flow. In order to do so, we have defined 3 analysis windows in different parts of the flow. Each window is defined by its center point in millimetres : I $(17, 52)_{X,Y}$, II $(31, 63)_{X,Y}$ and III $(49, 76)_{X,Y}$ and its size extension. The 3 points are represented in Fig. 4(l.). Moreover, Table 2 summarizes the main results obtained in the 3 analysis windows. The second column displays the area of each window (μm^2) and the sample size associated (total number of droplets). The third and fourth column show the distribution fit of the parameters n (number density of droplets) and D_i (centre-to-centre inter-droplet distance with respect to the nearest neighbour) respectively. $\mathbb{E}[X]$ and $SD[X]$ are respectively the expected value and the standard deviation of the variable X (either D_i or n). The fifth column introduces the D_i^{unif} parameter which designates the average inter-droplet distance if all droplets were uniformly distributed in the windows. The last column shows the corresponding distance parameter at each point.

To provide those results, a stack of Mie scattering images acquired at 1 kHz is used. Each image is indexed with the superscript "R" (for Repeated measurement). The stack height of images L^R is equal to 2 000 images. All the images are firstly processed by a tracking particle algorithm which provides the number of droplets by window N^R for each image "R". Since the droplet concentration in each window is different, the windows are sized to have a sufficient size sample as $N = \sum_{R=1}^{L^R} N^R > 10\,000$. A window dimension influence study is carried out by considering windows twice as large or twice as small and shows that the final results are not dependent of the window size. One defines the number density of droplets n^R as the ratio of the number of droplets N^R to the surface area of the window studied. Each counted droplet by window is indexed with the superscript "S" (for Sample).

A second algorithm assesses the Euclidean distance between all the droplets identified in the window. More especially, $D_i^{R,S}$ is defined as the centre-to-centre distance between the droplet "S" and its nearest neighbour in the window of image "R". In practice, this inter-droplet distance allows to describe the level of droplet-droplet interactions in a spray (alteration of droplet drag and vaporization rates). Thus, we define $\mathbb{E}[D_i]$ as the average of the nearest neighbour distances for all images and all droplets counted in the window :

$$\mathbb{E}[D_i] = \frac{1}{N} \sum_{R=1}^{L^R} \sum_{S=1}^{N^R} D_i^{R,S} \tag{2}$$

In order to compare the average inter-droplet distance measured experimentally $\mathbb{E}[D_i]$ to a reference droplet spacing, we define the D_i^{unif} parameter as the inter-droplet distance if all droplets were uniformly distributed in the windows. This theoretical parameter can be written as :

$$D_i^{unif} = \frac{1}{L^R} \sum_{R=1}^{L^R} [n^R]^{-\frac{1}{2}} \tag{3}$$

Firstly, from Table 2, one notes that the uniform distance is always greater than the average inter-droplet distance measured experimentally ($D_i^{unif} > \mathbb{E}[D_i]$). To go further into this observation, fit distributions are carried out from the statistics in number density and inter-droplet distance. Among a vast choice of probability density functions, the best distribution fitting - which minimizes the value of the Bayesian information criteron - is searched. The outcomes are displayed in Table 2. It appears that all the inter-droplet distance distributions follow positively skewed distributions, in particular Log-Normal. Therefore, those distributions are shifted towards the smallest value of inter-droplet distance. Likewise, the number density of droplets may be approximated with Log-Normal probability density functions. Even though a Gaussian distribution is obtained at the point I, the use of a Log-Normal distribution with a low skewness seems reasonable. In Fig. 6, distributions are fitted from the experimental histograms for the point II and one can see the goodness-of-fit. In conclusion, these results suggest that the assumption of homogeneous (or uniform) distribution of droplets made in analytical studies of spray combustion regimes can be refuted [1,3,5].

Table 2 – Outcomes of the experimental distributions of droplets - Reacting two-phase flow

Point	Window size (Sample size)	Distribution Fit [n] ($\mathbb{E}[X]$, $SD[X]$)	Distribution Fit [D_i] ($\mathbb{E}[X]$, $SD[X]$)	D_i^{unif}	$\bar{C} = \dfrac{\mathbb{E}[D_i]}{d_{10}}$
I	993 x 993 (38 000)	**Gaussian** (1929 , 393)	**Log-Normal** (178 , 61)	232	4
II	3319 x 3319 (56 100)	**Log-Normal** (258 , 125)	**Log-Normal** (365 , 217)	677	9
III	5673 x 5673 (27 900)	**Log-Normal** (44 , 30)	**Log-Normal** (860 , 721)	1745	24

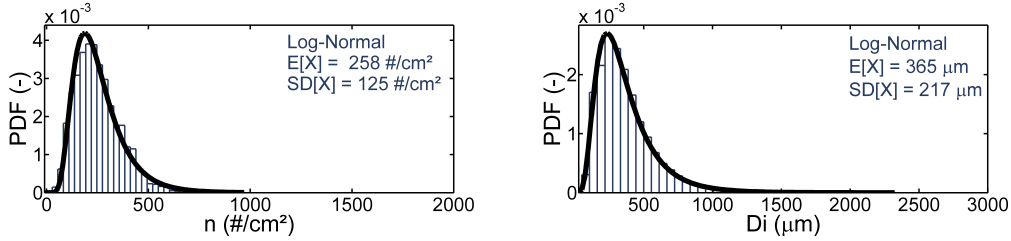| Window size (μm^2) | Sample size (# of droplets) | n (# of droplets /cm^2) | D_i (μm) | $\bar{C}$ (-) |

Figure 6 – PDF of the number density **(left)** and the inter-droplet distance **(right)** - Reacting two-phase flow - Point II

Secondly, from Table 2, another observation is that the number density decreases with the distance from the nozzle, and conversely the inter-droplet distance increases. We assume that there must be a dependence between those parameters. Consequently, we attempt to relate $\overline{D_i^R}$, defined as the average of the nearest neighbour distances for the image "R" (see Eq. (4)), and n^R the number density of droplets for the image "R". By doing so, we can formulate the dependence between those two parameters (see Eq. (5)).

$$\overline{D_i^R} \quad = \quad \frac{1}{N^R} \sum_{S=1}^{N^R} D_i^{R,S} \tag{4}$$

$$= \quad \alpha^R . [n^R]^{-\frac{1}{2}} \tag{5}$$

where α^R is a dimensionless proportional coefficient between 0 and 1. For instance, if the coefficient α^R is equal to unity, one finds the theoretical uniform distribution.

In order to conclude about the droplet clustering, the spatial distribution of droplets measured experimentally has been compared with a random distribution. For this purpose, a program including a pseudorandom number generator is implemented for generating random droplet positions in each window - whose dimensions are equal to the experimental ones. A lot of simulations, more than 5 000, are conducted to produce statistics on inter-droplet distances. Subsequently, by defining distinct classes of number density, a subroutine sorts the data and calculates an average inter-droplet distance per class $\mathbb{E}[D_i \mid n]$. In particular, $\mathbb{E}[D_i \mid n]$ is defined as the conditional expected value of inter-droplet distance knowing n and hence can be expressed by Eq. (6). Besides, in the subroutine, the number density of droplets, inside each window, varies from minimal to maximal values which are close to measured ones. In addition, this interval is arbitrarily cut in 6 classes. Finally, the subroutine assesses the coefficient $\alpha_{|n}$ from Eq. (7) in order to characterize the distribution.

$$\mathbb{E}[D_i \mid n] \quad = \quad \frac{1}{N_{|n}} \sum_{R=1}^{L^R_{|n}} \sum_{S=1}^{N^R_{|n}} D_i^{R,S} \tag{6}$$

$$= \quad \alpha_{|n}.n^{-\frac{1}{2}} \tag{7}$$

where $N_{|n}$, $N^R_{|n}$, $L^R_{|n}$ are respectively the total number of droplets, the number of droplets by window for the image "R" and the stack heigh of images and are all conditioned for a fixed n.

To compare those numerical calculations with the experiments, the same subroutine is used to process the experimental data. The variation of the average inter-droplet distance per class versus the inverse square root of the number density, at the point II, for the uniform, experimental and random distributions is plotted on Fig. 7. At first, it seems that for each distribution, the coefficient $\alpha_{|n}$ is constant. In order words, the proportional coefficient between $\mathbb{E}[D_i \mid n]$ and n is independent of the number of droplets in the window. So, from Table 2, one can obtain a good assessment of the experimental value of $\alpha_{|n}$ by solely determining the ratio of $\mathbb{E}[D_i]$ and D_i^{unif}. From Fig. 7, it appears no significant deviation of the spatial distribution of droplets between experimental and perfect random distributions. Equivalent outcome is found for the point III. In consequence, under those reactive conditions, there are no more neighbour droplets than random case. Consequently, no evidence of droplet clustering is observed within the flame. Therefore, droplets seem mainly scattered by random phenomena, such as turbulence, droplet collisions but not much influenced by additional causes - such as memory of the injection process nor particle inertia - which may lead to droplet clustering formation (or "patchiness") as suggested by Kotsinski [17]. In addition, from an experimental point of view, if the laser sheet is too thick compared to cluster spacing, then it is likely that an initially heterogeneous distribution (with evidence of droplet clustering) may be altered towards a seemingly more random distribution due to volume effects. In this study, the laser sheet is about 1 mm thickness. In consequence, future studies might try to asses this volume effect in order to definitively conclude about this far-reaching consideration.
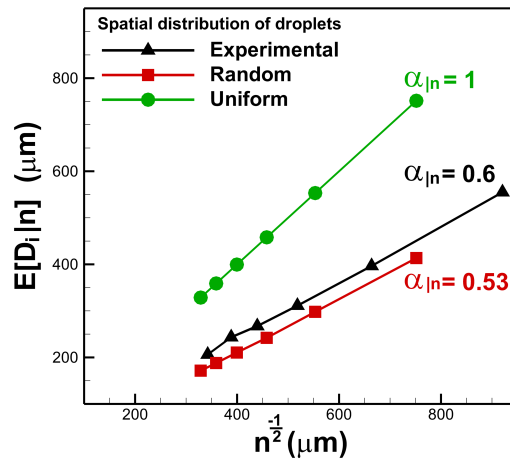

Figure 7 – Variation of the conditional average inter-droplet distance (μm) vs the inverse square root of the density number (μm) for different type of distributions [Random : $\alpha_{|n} = 0.53$ | Experimental : $\alpha_{|n} = 0.6$ | Uniform : $\alpha_{|n} = 1$] - Reacting two-phase flow - Point II

3.5 Spray Combustion Regimes

In section 2.3, we present the setting of optical diagnostics as OH-PLIF and Mie scattering imaging. The synchronization of both techniques permits to superimpose initially independent visualizations. Two pairs of images are presented in Fig. 8. The reaction zones are coloured in red. The droplets, in white, are all dilated about 3 px in order to be well visible. The locations of the three analysed points are also displayed. By using such superimposed images, detailed cross sections of the two-phase flow combustion are obtained.

Firstly, one observes that the number of droplets is relatively important just downstream the injector (around the point I) and within the recirculation zone (along the bottom part of the images). Furthermore, the number of droplets decreases significantly through the flame. Actually, in the top right of the images, there is almost no droplet.

Secondly, it seems that the flame is split into hot reactive pockets. The flame fronts are thick and wrinkled. There are also non-burning zones within the spray. This latter observation may be explained by too-rich-fuel zones - not enough oxidant compared to fuel vapour - which causes local flame extinctions. It should be noted that these behaviours are far different from a premixed pre-vaporized flame wherein the combustion is much more homogeneous [13-14].
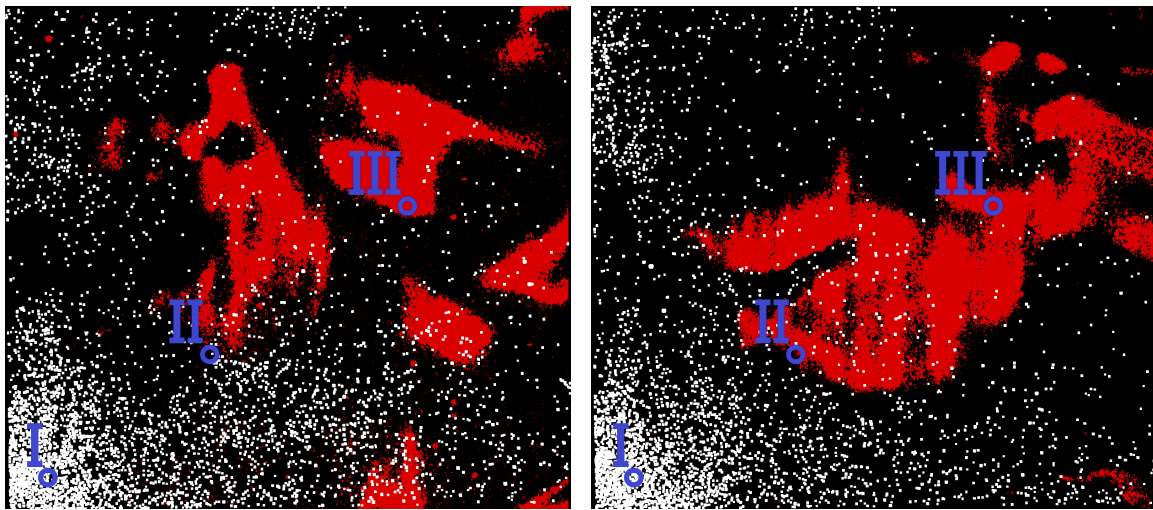

Figure 8 – Two typical images of simultaneous OH-PLIF and Mie scattering - Reacting two-phase flow

The different behaviours observed in this article seem supporting the existence of spray combustion regimes. For instance, near the nozzle, it seems that the droplets vaporize collectively without presence of reacting zones. In particular, as reported in Table 2, the distance parameter $\overline{C} = \mathbb{E}[D_i]/d_{10}$ is relatively small near the nozzle (equal to 4 at the point I). Since the number density is high, the collective droplet effects must be important and the blowing rate of fuel vapour may prevent the oxygen from penetrating into the spray. So, as seen in Fig. 4(l.) and 8, the flame is established downstream, outside the fuel feeding zone (beyond the point I). As a consequence, it seems that an "External Group Combustion" regime occurs.

As indicated in Table 2, the distance parameter increases from 4 (point I) to 9 (point II). Between these two points, another behaviour can be described. Indeed, from the time average of chemiluminescence images, Fig. 4(l.), we see that the flame is anchored beyond the point I. Thus, the point II appears inside the reacting zone. Nevertheless, from Fig. 8, the flame is mainly located beyond the point II. The fact is the chemiluminescence is a three-dimensional measurement since it integrates the OH* emissions on the whole depth of the combustor unlike OH-PLIF which is planar. So, between the point I and II, the droplets are collectively surrounded with the flame. Consequently, this behaviour seems rather similar to a "Group Combustion" regime.

From the radius of the point II, the droplet spray becomes much more diluted. From Fig. 8, one observes that beyond the point II, the flame succeeds to penetrate into the spray. It is probably due to higher oxygen concentration and a better mixing with the fuel vapour. Moreover, as indicated in Table 2, the distance parameter increases from 9 (point II) to 24 (point III). It has been disclosed that the level of droplet-droplet interactions becomes negligible for a distance parameter greater than 10 [3]. So, beyond the point II, droplets are far apart and individual droplet behaviour is expected. Nevertheless, the "Single Droplet Combustion" regime can not be really highlighted on the images. It is likely that one of the causes is lack of resolution on OH-PLIF images. Besides, beyond the radius of the point II, there is no obvious correlation between the droplet positions and the flame positions. Despite the furtive crossing of

isolated droplets in the reaction zones, it seems that the diffusion flame becomes mainly a gaseous phase combustion. In conclusion, it seems clear that the inter-droplet distance plays a major role in the appearance of these spray combustion regimes.

4. Conclusion

The challenge of this experimental work was to build a new database in a two-phase flow combustion in order to improve spray combustion modelling and to validate numerical simulations. For this purpose, at ONERA Fauga-Mauzac, a new air breathing propulsion test setup has been recently developed : Prométhée-LACOM. The configuration is rather academic but the main features of the flow in an actual aero-engine combustor are preserved. Moreover, because of its bi-dimensional design, the test setup is particularly suitable for optical diagnostics. In this paper, both non-reacting and reacting two-phase flow were investigated.

To characterize the non-reacting flow, simultaneous measurements on the gaseous phase (pressure fluctuations) and liquid phase (two-components PDI and high-speed Mie scattering by droplets imaging) were carried out. A spectral analysis from the pressure fluctuations just upstream the combustor revealed a narrowband peak frequency corresponding with a von Kármán vortex shedding. A phase-averaging was applied on the Mie scattering images and permitted to relate the unsteadiness of droplets dispersion with regards to the dynamic behaviour of the gaseous phase. Two PDI measurements sections were provided in order to define the injection conditions for numerical simulations (droplet sizes and velocities).

Likewise, a spectral analysis from the pressure fluctuations was conducted under reactive conditions. Nevertheless, we observed the complete vanishing of vortex shedding because of heat released by the combustion process. The same two PDI measurement sections were realized and compared with the non-reactive case. Firstly, differences on droplet size distributions were noticed. In the reacting flow, the smallest droplets were vanishing more rapidly than the increase of the evaporation of the biggest ones indeed. Through the flame, the droplet size decreased rapidly. Secondly, the droplets were accelerated in the reacting flow compared to the non-reacting flow. For instance, the average longitudinal velocity of droplets was multiplied by a factor 3 - corresponding approximatively with the ratio of density between both cases.

To characterize the spatial distribution of fuel droplets in the reacting flow, we used a large stack of Mie scattering images to perform statistical analysis. The results indicated that the centre-to-centre inter-droplet distance (nearest neighbour) can be described by means of a Log-Normal distribution. It can be concluded that the assumption of uniform distribution of droplets made in analytical studies of spray combustion regimes can be refuted. Furthermore, we generalized the dependency between the inter-droplet distance and the inverse square root of the number density by introducing a proportional coefficient (see Eq. (5)). No evidence of droplet clustering was observed within the flame. However, the findings suggest no significant deviation of the spatial distribution of droplets between experimental and perfect random distributions.

Simultaneous OH-PLIF and Mie scattering imaging were implemented in order to describe the flame structure. By using such superimposed images, detailed cross sections of the two-phase flow combustion were obtained. The different behaviours observed in this study seem to support the existence of spray combustion regimes. For instance, near the injector, the flame is established outside the fuel feeding zone because of a too-rich-fuel mixture. Within a less dense zone, it seems that a "Group Combustion" regime was observed. Further away, the inter-droplet distances become so important that droplets must be almost isolated. In conclusion, it seems clear that the spacing between droplets is one of the most important parameter to describe collective droplet effects (alteration of drag and vaporization rate) and the spray combustion regimes.

The work will go on with the post-processing of the experimental data in the lower part of the combustor. Due to the spray asymmetry, possible differences with the present results are expected. In addition, influence of the inter-droplet distance will be investigated with respect to the numerical evaporation models [18-19].

Acknowledgements

References

[1] Chiu H.H. and Kim H.Y. Group combustion of liquid fuel sprays. *AIAA* **21**, 1983.

[2] Chigier N.A. Group combustion models and laser diagnostic methods in sprays : a review. *Combustion and Flame* **51**, 127-139, 1983.

[3] Correa S.M. and Sichel M. The group combustion of a spherical cloud of monodisperse fuel droplets. *The Combustion Institute* **19**, 981-991, 1982.

[4] Annamalai K. and Ryan W. Interactive processes in gasification and combustion. Part I : Liquid drop arrays and clouds. *Prog. Energy Combust.* **18**, 221-295, 1992.

[5] Candel S., Lacas N., Darabiha N. and Rolon C. Group combustion in spray flames. *Multiphase Science and Techn.* **11**, 1-18, 1999.

[6] Reveillon J. and Vervisch L. Analysis of weakly turbulent dilute-spray flames and spray combustion regimes. *J. Fluid. Mech* **537**, 317-347, 2005.

[7] Akamatsu F., Mizutani Y., Katsuki M., Tsushima S. and Dae Cho Y. Measurement of the local group combustion number of droplet clusters in a premixed spray stream. *The Combustion Institute* **26**, 1723-1729, 1996.

[8] Akamatsu F., Hwang S.M. and Park H.-S. Evaluation of combustion mechanism of droplet cluster by simultaneous time-series measurements in premixed spray flame. *J. Ind. Eng. Chem.* **13**, 206-213, 2007.

[9] Beck C.H, Koch R. and Bauer H.-J. Identification of droplet burning modes in lean, partially prevaporized swirl-stabilized spray flames. *The Combustion Institute* **32**, 2195-2203, 2009.

[10] Beck C.H, Koch R. and Bauer H.-J. Investigation of the effetc of incomplete droplet prevaporization on NO_x emissions in LDI combustion systems. *J. Eng. for Gas Turbines and Power* **130**, 1-8, 2008.

[12] Bill R.G and Tarabanis K. The effect of premixed combustion on the recirculation zone of circular cylinders. *Combustion Science and Techn.* 39-53, 1986.

[13] Shanbhogue S.J., Hussain S. and Lieuwen T. Lean blowoff of bluff-body stabilized flames : scaling and dynamics. *Prog. in Energy and Combustion Science* **35**, 98-120, 2009.

[14] Chaudhuri S., Kostka S., Renfro M.W. and Cetegen B.M. Blowoff dynamics of bluff-body stabilized turbulent premixed flames. *Combustion and Flame* **157**, 790-802, 2010.

[15] Vicentini M., Lecourt R., Bodoc V., Rouzaud O. and Simonin O. Regimes de combustion dans les foyers aéronautiques : Mise en place expérimentale de l'écoulement diphasique. *Congrès Francophone des Techniques Laser* **14**, LV-5.1, 2014.

[16] Bachalo W.D. Spray diagnostics for the twenty-first century. *Atomization and Sprays* **10**, 439-474, 2000.

[17] Kostinski A.B. and Shaw R. A. Scale-dependent droplet clustering in turbulent clouds. *J. Fluid. Mech.* **434**, 389-398, 2001.

[18] Abramzon B. and Sirignano W. Droplet vaporisation model for spray combustion calculations. *Int. J. Heat and Mass Transfer* **9**, 1605-1618, 1989.

[19] Paulhiac D. Modélisation de la combustion d'un spray dans un brûleur aéronautique. *INP Toulouse PhD. Thesis*, 2015.